Solar Phys (2010) 261: 127–148
DOI 10.1007/s11207-009-9470-2

How Can a Negative Magnetic Helicity Active Region Generate a Positive Helicity Magnetic Cloud?

R. Chandra · E. Pariat · B. Schmieder · C.H. Mandrini · W. Uddin

Received: 30 March 2009 / Accepted: 5 October 2009 / Published online: 13 November 2009

Abstract The geoeffective magnetic cloud (MC) of 20 November 2003 was associated with the 18 November 2003 solar active events in previous studies. In some of these, it was estimated that the magnetic helicity carried by the MC had a positive sign, as did its solar source, active region (AR) NOAA 10501. In this article we show that the large-scale magnetic field of AR 10501 has a negative helicity sign. Since coronal mass ejections (CMEs) are one of the means by which the Sun ejects magnetic helicity excess into interplanetary space, the signs of magnetic helicity in the AR and MC must agree. Therefore, this finding contradicts what is expected from magnetic helicity conservation. However, using, for the first time, correct helicity density maps to determine the spatial distribution of magnetic helicity injections, we show the existence of a localized flux of positive helicity in the southern part of AR 10501. We conclude that positive helicity was ejected from this portion of the AR leading to the observed positive helicity MC.

R. Chandra (✉) · B. Schmieder
Observatoire de Paris, LESIA, UMR8109 (CNRS), 92195 Meudon Principal Cedex, France
e-mail: chandra.ramesh@obspm.fr

B. Schmieder
e-mail: brigitte.schmieder@obspm.fr

E. Pariat
NASA-GSFC, Space Weather Laboratory, 8800 Greenbelt Rd, Greenbelt, MD 20771, USA
e-mail: epariat@helio.gsfc.nasa.gov

E. Pariat
College of Science, George Mason University, 4400 University Dr., Fairfax, VA 22030, USA

C.H. Mandrini
Instituto de Astronomía y Física del Espacio (IAFE), CONICET-UBA, Buenos Aires, Argentina
e-mail: mandrini@iafe.uba.ar

W. Uddin
Aryabhatta Research Institute of Observational Sciences (ARIES), Nainital 263 129, India
e-mail: wahab@aries.ernet.in

Keywords Active regions; magnetic fields · Coronal mass ejections; interplanetary · Flares; dynamics, relation to magnetic field · Helicity; magnetic

1. Introduction

Magnetic helicity globally quantifies the signed amount of twist, writhe, and shear of the magnetic field in a given volume (see the review by Démoulin, 2007 and references therein). Magnetic helicity plays an important role in magnetohydrodynamics (MHD) because it is one of the few global quantities that are conserved, even in resistive MHD on time scales shorter than the global diffusion time scale (Berger, 1984).

Coronal mass ejections (CMEs) are expulsions of mass and magnetic field from the Sun. Rust (1994) and Low (1996) pointed out that one of the most important roles of CMEs is to carry away magnetic helicity from the Sun. Otherwise helicity will accumulate continuously. This is because helicity dissipates very slowly and helicities of opposite signs are globally injected through the photosphere in each solar hemisphere without a change of sign during consecutive cycles (Berger and Ruzmaikin, 2000). A fraction of CMEs can be observed *in situ* as magnetic clouds (MCs). An MC is characterized by lower proton temperature and higher magnetic field strength than the surrounding solar wind. Typically, the magnetic field vector shows a smooth and significant rotation across the cloud (Burlaga *et al.*, 1981; Klein and Burlaga, 1982). This indicates a helical (flux rope) magnetic structure, which clearly has nonzero helicity. Therefore, a measurable prediction is that the interplanetary MC must carry the same amount of helicity that was ejected from the solar source region. In particular, the signs of the magnetic helicity of the MC and of the solar region from which it originates should agree.

As a first approach, the magnetic helicity sign of some structures in the solar atmosphere can be inferred from certain observed morphological features (see the review by Démoulin and Pariat, 2009 and references therein). These features include *sunspot whorls* (handedness of the spiral patterns of chromospheric fibrils), *filament barbs* (direction of the barbs relative to the orientation of the magnetic field), *flare-ribbons* (forward/reverse "J-shape"observed in Hα and UV wavelengths), *sigmoids* (normal or reverse "S-shaped" loops in soft X-ray observations), *magnetic tongues* (angle formed by the magnetic inversion line relative to the AR axis in emerging ARs), *coronal loops* (orientation of loops in extreme ultraviolet (EUV) observations relative to the magnetic inversion line), and *vector magnetic field* (direction of sheared fields). These observational features can be used to qualitatively compare the magnetic helicity sign of an MC with that of its solar source, once it is identified (*e.g.*, Subramanian and Dere, 2001; Schmieder, and van Driel-Gesztelyi, 2005; Ali *et al.*, 2007). In a similar way, *i.e.*, directly from observations, the helicity sign of MCs can be estimated from the measured rotation of the vector magnetic field (see examples in Bothmer and Schwenn, 1994, 1998).

Several studies found that the magnetic helicity sign of the MC and that inferred from the morphological features of its source AR match (*e.g.*, Rust and Kumar, 1994; Bothmer and Schwenn, 1994, 1998; Marubashi, 1997; Ruzmaikin, Martin, and Hu, 2003; Rust *et al.*, 2005). Other studies determined the helicity sign of the CME source region modeling the coronal magnetic field (*e.g.*, Yurchyshyn *et al.*, 2001, 2006); in these cases the source region and cloud helicity signs were also in agreement. However, the comparison does not yield a complete agreement since some of the MCs seem to present a different helicity sign from that of their solar source (Leamon *et al.*, 2004).

Quantitative comparisons of the helicity involved in the solar ejection and that of the associated MC have recently been made possible. In the interplanetary medium, these quantitative comparisons require either the modeling of *in situ* magnetic field observations (see the reviews by Dasso *et al.*, 2005 and Nakwacki *et al.*, 2008) or, in cases where the impact parameter is small and considering a local cylindrical geometry, the MC helicity can be directly quantified from the data (Dasso *et al.*, 2006). In the solar atmosphere at least two different methods, giving consistent results (Lim *et al.*, 2007), allow the estimation of the amount of ejected helicity. One way to do this is to compute the helicity variation before and after the ejection of the solar source region using a coronal field model (Green *et al.*, 2002; Démoulin *et al.*, 2002; Mandrini *et al.*, 2005; Régnier, Amari, and Canfield, 2005; Luoni *et al.*, 2005). This method requires the knowledge of the magnetic field in the entire volume. Another way is to measure the helicity injection based on a time series of photospheric field observations. This was initiated by Chae *et al.* (2001) and Chae (2001) and was subsequently applied to the study of CMEs by Nindos and Zhang (2002) and Nindos, Zhang, and Zhang (2003). Pariat, Démoulin, and Berger (2005) showed that, although the methods used in previous work can correctly estimate the total injected flux of helicity, they incorrectly determine the localized injected flux. They thus proposed an alternative to properly map the helicity flux injection. We shall use this corrected method to compute the magnetic helicity injection in AR 10501.

The large MC observed on 20 November 2003 gave place to the largest geomagnetic storm of Solar Cycle 23 (Gopalswamy *et al.*, 2005). This MC was associated with the active solar events that occurred in AR 10501 on 18 November 2003 by several authors (Gopalswamy *et al.*, 2005; Yurchyshyn, Hu, and Abramenko, 2005; Möstl *et al.*, 2008). The association discussed by Gopalswamy *et al.* (2005) was mainly based on the timing between the filament ejections in AR 10501, the appearance of CMEs in the Large Angle and Spectroscopic Coronagraph (LASCO) white-light images (its height-time plots), and the arrival of the MC to the Advanced Composition Explorer (ACE) spacecraft and its velocity. Yurchyshyn, Hu, and Abramenko (2005) also estimated the AR helicity sign modeling the AR coronal magnetic field and the MC *in situ* data; the latter authors showed that the helicity of the MC and AR were both positive. However, Möstl *et al.* (2008) discussed that, while the MC helicity sign seems well determined, the handedness (or helicity sign) of the very extended filament, lying along different portions of the inversion line within and in the surroundings of the AR, is ambiguous.

In this article, we revisit the evolution of the activity in AR 10501 along 18 November 2003 in Section 2. Then, we discuss the characteristics of the positive-helicity-carrier MC observed by ACE on 20 November 2003 and its association with the CMEs originating from the AR (Section 2.3). To verify this association, we carefully analyze the morphological features of the region; in particular, the different segments of filament material lying along the magnetic inversion line that are observed as forming a single and very extended filament. We find that all these observational features, except for one filament segment, indicate that the sign of the dominant helicity in the AR is negative. Global magnetic field extrapolations, before any AR activity, agree with this finding (Section 4). This strongly contradicts what is expected of models of MC formation constrained by the helicity conservation principle. In view of this result, we analyze the photospheric magnetic field evolution of the region and we perform an in-depth analysis of the local helicity flux injection along 18 November (Section 6). We find that a zone at the south of AR 10501 is the location of positive helicity flux injection during that day. Finally, we conclude that the ejected flux rope, observed later as an MC, should be located at this southern portion of the AR, and discuss the implications of our finding for CMEs/MCs triggering models (Section 7).

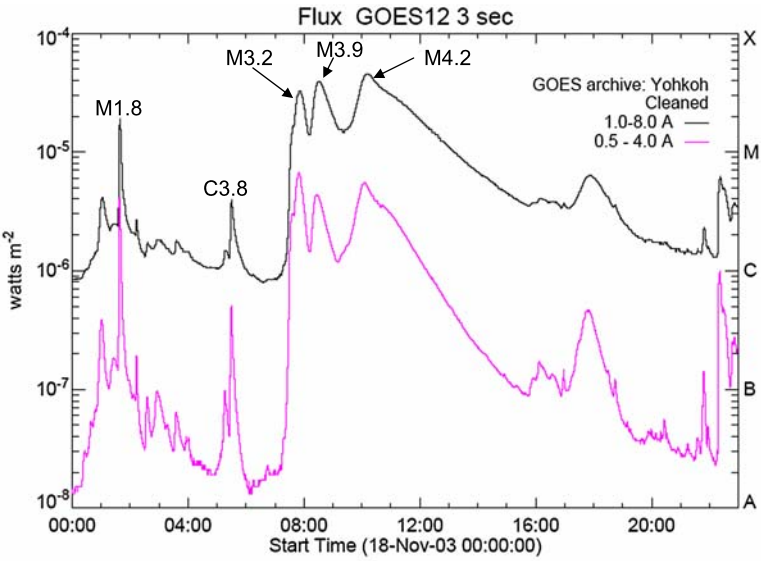

Figure 1 Temporal evolution of the X-ray solar flux observed by GOES 12 in the 0.5 – 4 Å and 1 – 8 Å bandwidths on 18 November 2003.

2. Observations of AR 10501 Activity

2.1. Temporal Evolution of the Flares

The decay phase of Solar Cycle 23 was marked with an unexpected extreme level of activity, the so-called Halloween events. Figure 1 shows the temporal evolution of the flares observed by Geostationary Operational Environmental Satellite (GOES) on 18 November 2003. Five flares occurred on this day. Three of them, viz. the C3.8/SF at 05:25 UT, M3.2/2N at 07:52 UT, and M3.9/2N at 08:30 UT flares (in terms of X-ray/Hα classes) were observed to originate from AR 10501 (located at N03E08). These flares will be hereafter referred to as the first, the second, and the third flares, respectively. These flares were associated with filament eruptions.

The M3.2 and M3.9 flares were associated with two CMEs, detected by LASCO (Brueckner *et al.*, 1995). The first CME was detected in the C2 field-of-view at 08:06 UT, had a speed of $\approx$1223 km s^{-1}, and a width of 104°. The second halo CME was observed at 08:50 UT with a speed of $\approx$1660 km s^{-1} (see http://cdaw.gsfc.nasa.gov/CME_{list}/).

2.2. Filament Eruptions

For this work, we use the Hα data from the Aryabhatta Research Institute of Observational Sciences (ARIES), Nainital, India, obtained with the 15 cm $f/15$ coudé tower telescope equipped with an Hα Halle filter having a pixel size of 1″. We also use magnetograms acquired with the Michelson Doppler Imager (MDI, onboard the Solar and Heliospheric Observatory (SOHO), time cadence of 96 minutes and pixel size of 1.98″; Scherrer *et al.*, 1995) and 171 Å/1600 Å images obtained with the Transition Region and Coronal Explorer (TRACE, pixel size of 0.5″; Handy *et al.*, 1999).

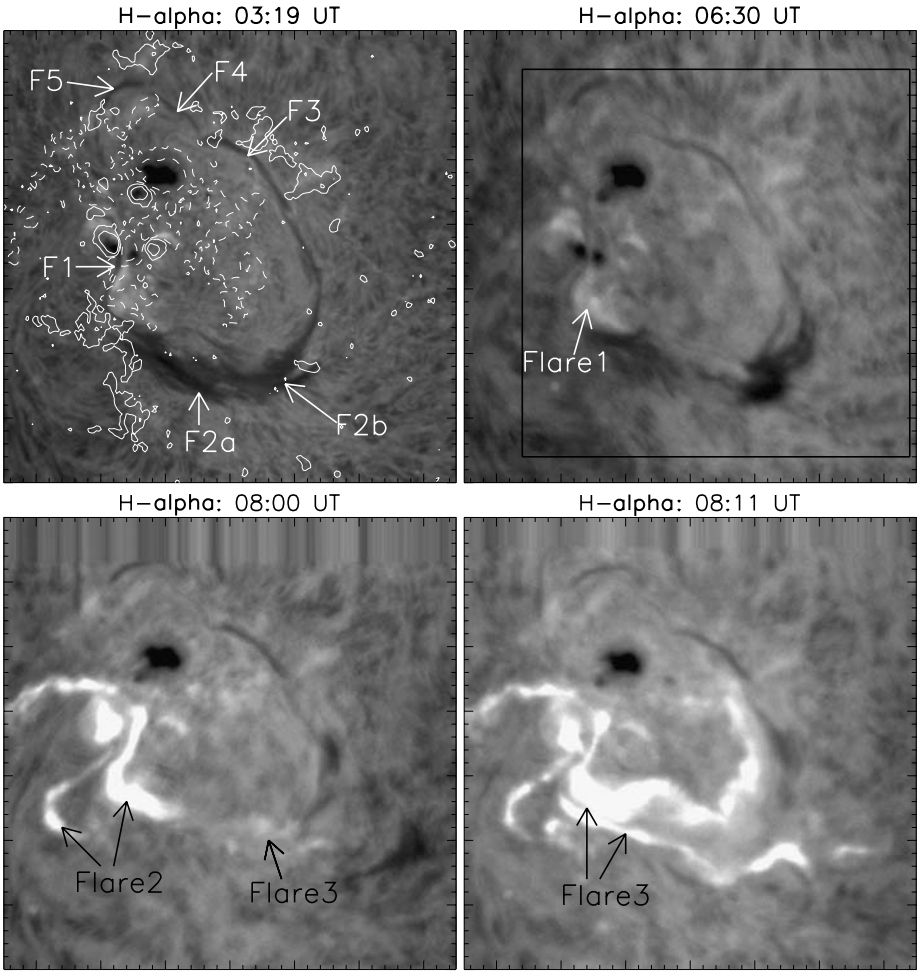

Figure 2 Hα images before (top left panel), after the first (top right panel), and during second (bottom left panel), and third (bottom right panel) flare. The field-of-view of the all the images is $350'' \times 350''$. Top left: Hα image overlaid by MDI magnetic field contours. The ± 100 and ± 500 G (gauss) isocontours of the positive and negative line-of-sight magnetic fields are plotted with solid and dashed lines, respectively. The arrows indicate the different filament segments. The arrows in the other panels point to the three flare ribbons. The square on the top right panel shows the field-of-view of the images presented in Figure 3. The arrow in the bottom left panel points to the two faint brightenings which correspond to the onset of the third flare.

All images, Hα, TRACE, and MDI magnetograms, are coaligned to compare the different observed features. Figure 2 shows Hα images before (top left image overlaid with MDI line-of-sight isocontours on 18 November 2003 at 06:23 UT) and during the three flares mentioned previously. This AR is formed by a large negative-polarity spot, surrounded by weaker positive polarities. Along the inversion line, different segments of filament material encircle the main negative polarity forming an apparent large circular-shaped single filament. The circular-shaped filaments were also studied in previous articles (Rompolt, 1990; Schmieder *et al.*, 2007). Indeed, a filament may consist of different sections or segments in complex ARs (Deng *et al.*, 2002). Filament models showed that several magnetic flux tubes

sometimes have to be introduced to reproduce the observed distribution of filament material (Bobra, van Ballegooijen, and DeLuca, 2008; Dudík *et al.*, 2008). The different segments of the present filament are identified and numbered as follows (see Figure 2, top left panel): F1 is in the east, F2 with a gap between F2a and F2b in the south, F3 in the northwest, F4 and F5 in the north. The Hα image at 06:30 UT (Figure 2, top right) shows the segment F1 lying between two small spots south of the main spot, F2a has a large extension toward east and F2b a dark extension toward west. Actually, F2a and F2b may be two separate filaments. This decomposition of F2 into two segments is also consistent with the different chirality of each section, as detailed in Section 3. Nevertheless, we keep the F2 notation for both segments since the Hα movie reveals a counterstreaming motion along F2 and some plasma traveling in the east-west direction several times during the pre-eruptive phase. Counterstreaming in such a huge filament is a signature of instability (Schmieder *et al.*, 2008). F3, F4, and F5 are visible as faint spines. At 08:00 UT (Figure 2, bottom left panel), after the first and second flares, F1 and F2a are no longer visible and F2b is erupting (black structure in the right part of the frame). Simultaneously, bright flare ribbons develop on both sides of the filament channel of F1. Weaker brightenings then appear along the filament channel of F2a and F2b. This location is the place where the onset of the third flare begins (Figure 2, bottom right panel). These ribbons are well observed in TRACE 1600 Å images (Figure 3). The ribbons expand away from the polarity inversion line as the flare progresses. The flare ribbons of the third flare develop toward east and join the flare ribbons of the second flare to make a unique system of two ribbons. Figure 3 (bottom right) presents a TRACE 171 Å image of the post-flare loops overlaid by MDI magnetic field contours. The filament segments F3, F4, and F5 are not affected by the different flares, the eruption of F2, or the disappearance of F1.

2.3. Associated Magnetic Cloud on 20 November 2003

The interplanetary cloud associated with the 18 November 2003 solar active events lasted from 11:16 UT to 18:44 UT on 20 November 2003 when observed at ACE, according to Mošt*l et al.* (2008). In order to identify which of the filament ejections can be at the origin of this MC, we proceed as suggested by Démoulin (2008) in his review. He pointed out that, when associating solar to interplanetary events using their observation times, it is more reliable to start from the time at which the MC is observed and to extrapolate backward to the solar surface. This is because first, *in situ* radial velocities are more precise and second, these velocities are closer to the mean velocity during the travel time of the cloud than the plane-of-sky velocities measured using coronagraph data.

From ACE data, the MC mean radial velocity is $\approx$600 km s^{-1}. If we extrapolate it back to the solar surface, *i.e.*, 1 AU distance, the solar ejection should have occurred 69 hours before. Taking $\approx$15:00 UT as the time for the MC center passing across ACE, the solar source event should have occurred at $\approx$18:00 UT on 17 November. The solar source can be searched in a time window as long as $\pm$1 day, as used in some studies (Marubashi, 1997; Watari, Watanabe, and Marubashi, 2001). Then, we search from 16 November, 18:00 UT, to 18 November, 18:00 UT on the Sun. We find four CMEs on 17 November (*i.e.*, at 08:50 UT, 09:26 UT, 13:50 UT, and 23:50 UT) and four CMEs on 18 November (*i.e.*, at 05:26 UT, 08:06 UT, 08:50 UT, and 09:50 UT). It is generally believed that an MC will be observed in the vicinity of Earth if its associated CME is a halo or a partial halo and if its source region is close to the solar disk center. Therefore, as also proposed by Gopalswamy *et al.* (2005), the most probable solar source for the MC is the CME of 18 November 2003 at 08:50 UT. This is a halo CME that is associated with the largest flare and eruption from AR 10501, located close to the solar disk center at that time.

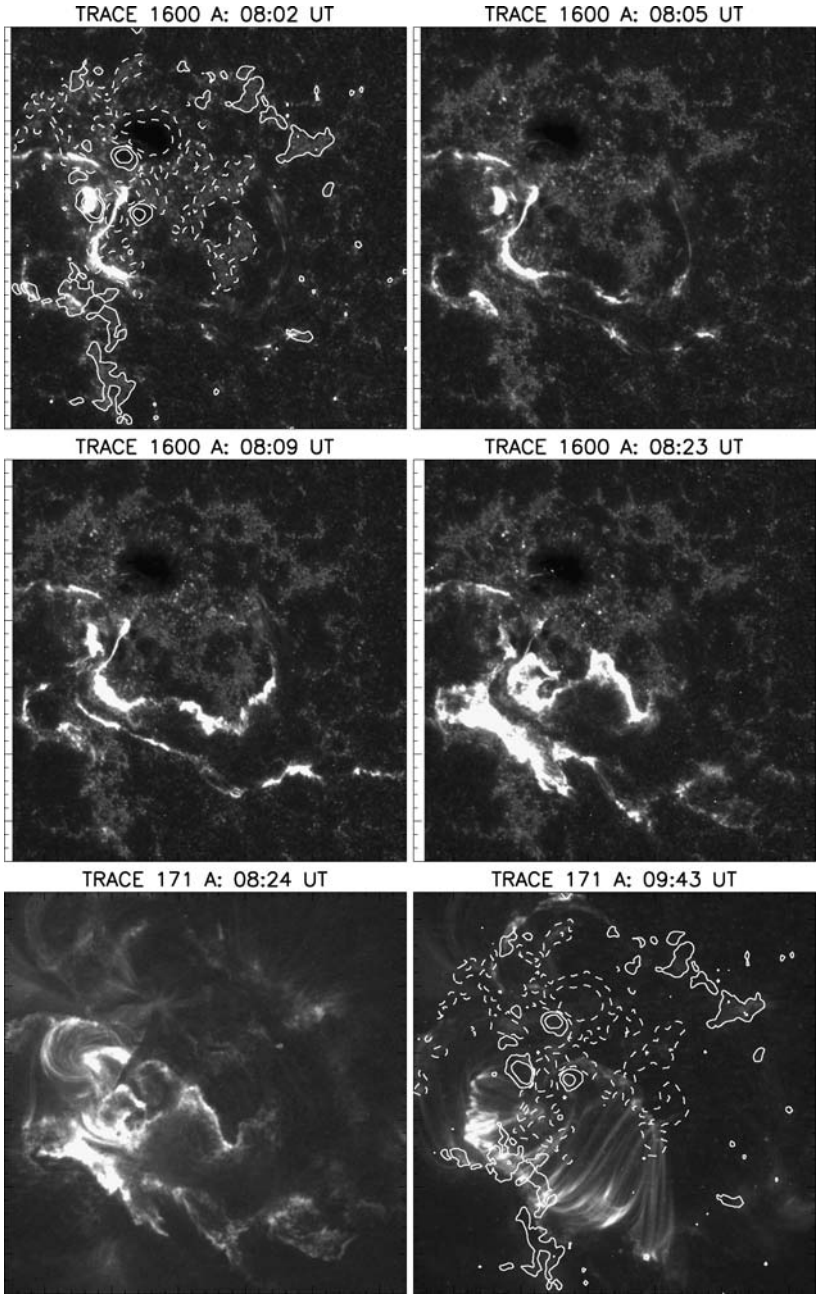

Figure 3 Upper and middle panels: TRACE 1600 Å images of the second and third flares. The upper-left image is overlaid by MDI magnetic field contours (dashed/solid lines correspond to negative/positive values). Bottom panels: TRACE 171 Å images of the third flare during the maximum and decay phase. The right image is overlaid by MDI contours (dashed/solid lines correspond to negative/positive values). The isocontours of the line-of-sight magnetic field are ± 100 and ± 500 G. The field-of-view of the images is $300'' \times 300''$.

Different aspects of the MC of 20 November 2003 were studied by several authors (Yurchyshyn, Hu, and Abramenko, 2005; Gopalswamy *et al.*, 2005; Wang *et al.*, 2006; Möstl *et al.*, 2008); all of them concluded that the MC helicity was positive and that its source region was AR 10501. In particular, its magnetic helicity sign can be directly determined from observations (see Figure 7 in Yurchyshyn, Hu, and Abramenko, 2005). That is, from the magnetic field components in the geocentric solar ecliptic (GSE) system of coordinates it can be seen that this is an East-South-West (ESW) cloud (see Bothmer and Schwenn, 1994), indicating a positive magnetic helicity.

3. Helicity Deduced from Observed Morphological Features of NOAA AR 10501

As discussed in Section 1, the magnetic helicity sign of an AR can be deduced from several observed morphological features (Démoulin and Pariat, 2009). Figure 4 shows an Hα image of AR 10501 illustrating the structures from which the helicity sign can be inferred.

1. *Sunspot Whorls:*

   The curvature of the fibrils around sunspots can be used as a tracer of the helicity sign in an active region (Nakagawa *et al.*, 1971; Rust and Martin, 1994; Chae, 2001) since the direction of the fibrils is related to the twist of the sunspot magnetic field. A sunspot in which the fibrils turn counterclockwise (clockwise) toward it will have negative (positive) magnetic helicity, respectively. In AR 10501, the fibrils around the main spot appear as counterclockwise whorls. This indicates that negative magnetic helicity is carried by the main spot.

2. *Shape of Flare Ribbons:*

   The double forward/reverse "J-shaped" ribbons and their orientation and displacement along the polarity inversion line indicate the magnetic helicity sign of the region (Démoulin, Priest, and Lonie, 1996; Pevtsov, Canfield, and Zirin, 1996). In Chandra *et al.* (2009), J-shaped ribbons were associated with the emerging flux of positive magnetic helicity. If we look at Figure 3 (top left), we find reverse-J-shaped flare ribbons. This can indicate that the AR globally has a negative magnetic helicity. However, the reverse-J-shaped flare ribbons follow the magnetic polarity inversion line. Therefore, flare ribbons may be a false indicator.

3. *Filament Segments and Barbs:*

   Gopalswamy *et al.* (2005) proposed a method to determine the magnetic helicity based on the sign of the magnetic polarities of both filament ends and on the direction of the field within the filament. Considering one end in the positive polarity (the northern end of F3) and the other end in the negative polarity (the southern end of F1), they derived a positive sign for the magnetic helicity of the filament material between these ends. Möstl *et al.* (2008) discussed the choice of the ends of the eruptive filament material and concluded that a negative helicity will be the correct one for the filament if two filaments are considered and not a unique circular filament.

   The chirality of a filament can also be directly inferred from the relative orientation of the barbs, *i.e.*, the fine structures along the filament spine (Zirker *et al.*, 1997; Martin, 1998). Tandberg-Hanssen (1994) described this method as follows: assuming that the filament spine corresponds to a "high-speed highway in the United States," the barbs of a dextral (sinistral) filament appear as a right (left) exit, respectively. In the simplest cases,

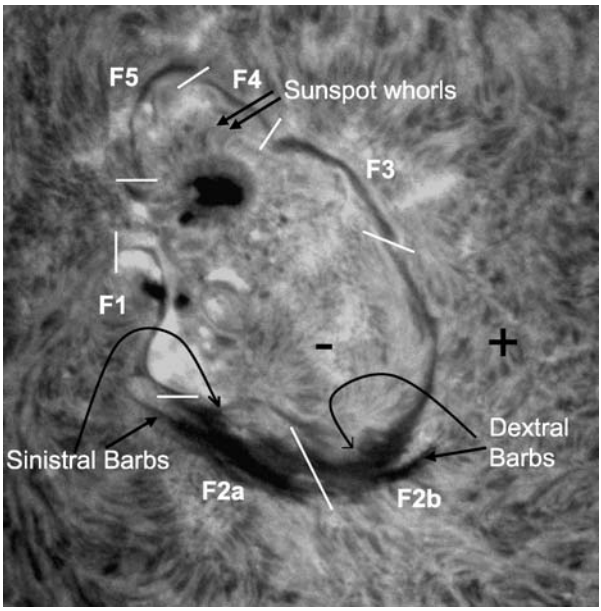

Figure 4 Hα image from ARIES (Nainital, India) of AR 10501 on 18 November 2003, at 03:19 UT, before the flares and eruptions of filament material (the + and − signs indicate the positive and negative polarity regions. The white bars indicate the ends of the different segments of the large-scale circular filament: F1, F2a, F2b, F3, F4, F5).

the filament has, in general, the same chirality as the associated AR (Lim and Chae, 2009). However, filaments may not be simple magnetic structures (*cf.* Section 1), and moreover, each segment of a filament may possess a different chirality, as was already observed by Martin, Bilimoria, and Tracadas (1994) and Schmieder *et al.* (2004) and modeled by DeVore, Antiochos, and Aulanier (2005). These works demonstrated that the segments cannot really merge if they have different chiralities, unlike segments that have the same chirality.

A filament in which the barbs, when viewed by an observer on the positive magnetic polarity side of the filament, are directed rightward (leftward) is called dextral (sinistral) and has a negative (positive) magnetic helicity, respectively. The overlying flux tube arcades, which are anchored in enhanced magnetic polarities on both sides of the magnetic inversion line, are left bearing (right bearing) in the case of negative (positive) helicity, respectively (Martin, 1998).

In the present active region, F1 has no visible barbs while F2 barbs are well identifiable (see Figure 4). In the eastern (F2a) part of this filament segment the barbs seem to correspond to a sinistral filament, while its western part (F2b) to a dextral filament. The filament segment F2 will thus have two sections of opposite magnetic helicity. Again, this determination remains relatively ambiguous. To confirm these observations other methods – extrapolation and computation of magnetic helicity – need to be used (see Sections 4, 5, and 6). The filament segment F2, where counterstreaming occurs, can be modeled by a flux tube with two different sections having the same central axis direction, but with opposite twists in F2a and F2b.

4. Evolution and Model of the Magnetic Field in AR 10501

The magnetic field evolution of AR 10501 before the flares and filament eruptions on 17 and 18 November is presented in Figure 5. AR 10501 is a decaying active region, the return of

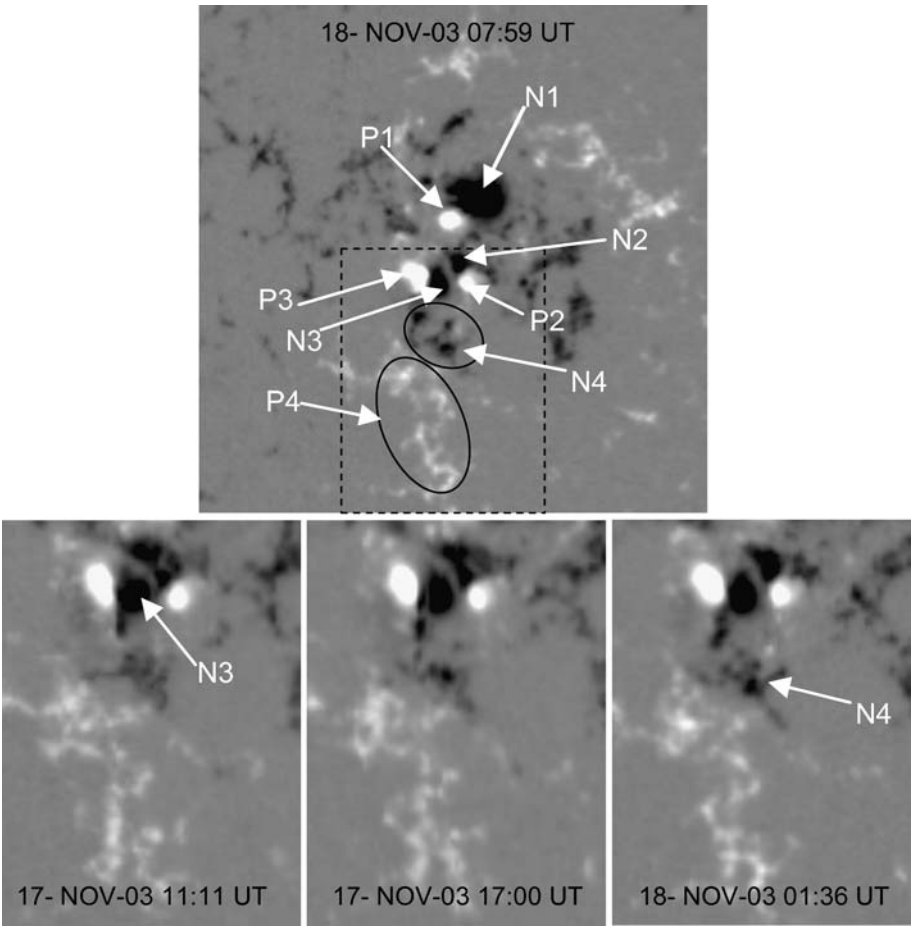

Figure 5 Top panel: SOHO/MDI magnetogram of AR 10501 on 18 November 2003, before flare onset. The different polarities are pointed by arrows (P1, P2, P3, P4: positive polarities and N1, N2, N3, N4: negative polarities). Bottom panel: enlarged view of the rectangular area on the top panel showing the evolution of parasitic polarities.

the very flare productive AR 10484 during October and November 2003. The AR is formed by several magnetic polarities, *viz.* P1, P2, P3, P4 (positive polarities) and N1, N2, N3, N4 (negative polarities), as marked in the upper panel of Figure 5. In the period preceding the events studied in this article, we observe the displacement of several small positive and negative polarities toward the south of the AR. These polarities break from the main AR spot and go away from it. These are the so-called moving magnetic features, typically observed during the decay stage of spots as they diffuse. The small polarities merge with others of the opposite sign as they move away from the spot. After 19 November, the negative polarity N2 breaks into two parts and both broken parts are seen to rotate around P3. On 20 November 2003, P2 and N2, which are fading, are no longer visible.

We extrapolated the photospheric magnetic field to the corona before the flares using a linear force-free-field approximation ($\nabla \times \mathbf{B} = \alpha \mathbf{B}$, where $\mathbf{B}$ is the magnetic field). We do this model using as the boundary condition a magnetogram at 06:23 UT on 18 November,

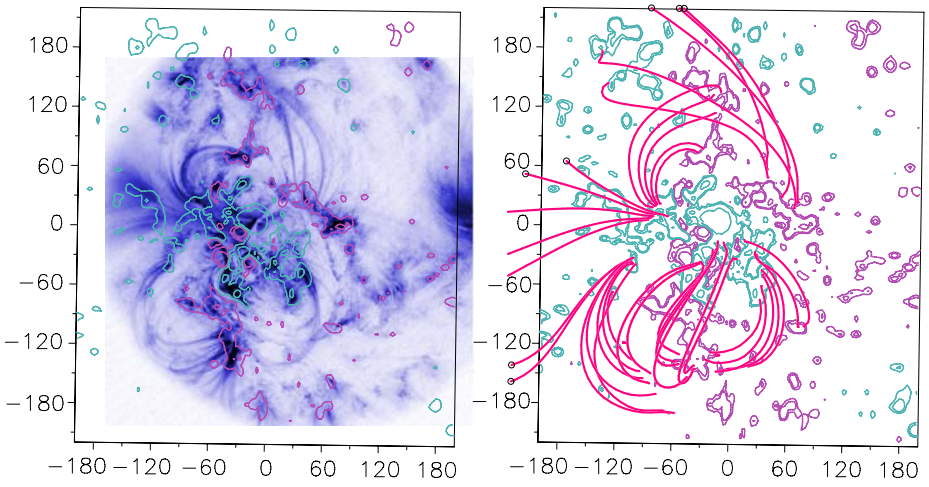

Figure 6 TRACE (171 Å, 05:24 UT) overlaid by SOHO/MDI contours (at 06:23 UT) (left) and field lines tracing the observed loops (right), computed from linear force-free-field models with different values of the α parameter (see text for details). The contours correspond to ± 50, ± 100, and ± 500 G (red for positive and cyan for negative polarities).

slightly earlier than the events discussed in Section 2. The value of the free-parameter of the model α is set by matching the shape of the computed field lines to that of observed coronal loops, as discussed in Green *et al.* (2002). The TRACE image in 171 Å at 05:24 UT, the closest in time to the MDI magnetogram, is used to select α. This image allows us to clearly observe the shape of the large-scale coronal loops (see Figure 6, left panel). The result of our model compared to TRACE loops is shown in Figure 6, right panel. We are not able to match all loops using a single value of α that is expected since, in general, the magnetic field is not a linear force-free field. Therefore, different sets of loops are modeled using different values for α. However, all the values needed to find the best match turn out to be either zero (for field lines anchored on the central eastern weak negative polarity and going away from the AR) or negative: the values of α being in the range $[-1.2, -0.6] \times 10^{-2}$ Mm^{-1}. These negative values of α correspond to a negative magnetic helicity. Therefore, the extrapolation of the magnetic field also confirms that the large-scale magnetic field of AR 10501 has a negative helicity sign, probably dominated by the negative helicity of the main AR bipole (N1/P1) (see Section 6).

Yurchyshyn, Hu, and Abramenko (2005) modeled the "post-flare" arcade after the two-ribbon flare (third flare) that peaked at 08:31 UT. In order to determine the value of α, these authors compared their computed field lines to the half-resolution 195 Å image obtained by the Extreme-Ultraviolet Imaging Telescope (EIT) at 09:36 UT (see their Figure 6). Yurchyshyn, Hu, and Abramenko (2005) found that the value of α that best matched the EIT loops was slightly positive. This result led them to conclude that the MC and AR helicity signs were in agreement.

We also modeled the post-flare arcade loops, but in this case we compared our computed field lines to the 171 Å TRACE image at 09:43 UT (see Figure 3, bottom right panel). This image has a resolution four times better than the EIT image used by Yurchyshyn, Hu, and Abramenko (2005) and the arcade loops can be seen more clearly. At the beginning of the flare the arcade loops are anchored at P4 and N4, as shown by the Hα bright ribbons in Figure 2 bottom panels. However, as the flare progresses and the Hα ribbons separate, only

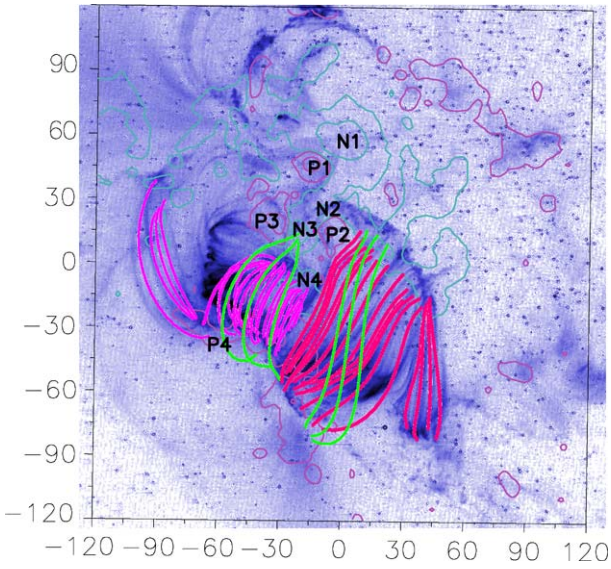

Figure 7 The TRACE image (171 Å, 09:43 UT) overlaid by SOHO/MDI contours (at 09:35 UT) and field lines tracing the observed 'post-flare' arcade loops. These have been computed using linear force-free models with different values of the α parameter (see text for details). The contours correspond to ± 100 and ± 500 G (red for positive and cyan for negative polarities).

the eastern portion of the arcade remains rooted in P4 and N4. This is probably due to the presence of the strong polarities P2 and N2 that hinder the ribbon separation (see Figure 3, bottom right panel). The western portion of the arcade, as also indicated by the location of the Hα ribbons, is still anchored in P4, whereas its negative footpoint lies on the weak field region to the west of P2. Figure 7 shows the result of our model overlaid on the TRACE image at 09:43 UT. The arcade loops to the east, anchored at P4 and N4, are represented by the set of pink field lines. These field lines are computed using either a potential field model or a positive value of $\alpha = 6 \times 10^{-3}$ Mm^{-1}. We want to remark that we are not able to model the loops located to the north of this set of field lines. We believe that they are part of the post-flare arcade corresponding to the first flare. The arcade loops to the west are represented by the set of red field lines; these field lines are computed using a negative value of $\alpha = -6 \times 10^{-3}$ Mm^{-1}. Since a linear force-free-field model can effectively represent the observed loops when they have a scale size of the order of α^{-1} (see Démoulin *et al.*, 1997), we argue that the short eastern loops can be modeled using either a low positive, negative, or null α value. To show that there exists a tendency for a positive value toward the east and negative toward the west part of the arcade, we also show a set of larger scale pink field lines anchored at P4 and at a northern negative polarity region for which $\alpha = 6 \times 10^{-3}$ Mm^{-1}. Though these field lines do not belong to the arcade, they clearly show that loops anchored at P4 have a tendency for positive magnetic helicity. This is in agreement with our finding of a sinistral filament segment (F2a) toward east, mainly along the inversion line between P4 and N4, and a dextral filament segment (F2b) toward west, mainly along the inversion line between weaker field polarities (not numbered in Figure 5). For comparison, and also to show the way the arcade field lines will evolve as the field relaxes to a potential state, we add a set of potential ($\alpha = 0$) field lines drawn in light green above both the eastern and western portions of the post-flare arcade. These results show that the AR magnetic helicity can be locally positive, as we also demonstrate in Section 5.

5. Photospheric Flux of Magnetic Helicity Flux in AR 10501

Recent theoretical developments and improvements in magnetic field measurements allow us to quantitatively determine the amount of magnetic helicity injected in an active region (see the review by Démoulin and Pariat, 2009).

5.1. Method

In order to compute the helicity flux injected in AR 10501, we determine the proxy for the helicity flux density, G_θ, at the position $\mathbf{x}$, as suggested by Pariat, Démoulin, and Berger (2005);

$$G_\theta(\mathbf{x}) = -\frac{B_\mathrm{n}}{2\pi}\int_{S_\mathrm{p}} \frac{\mathrm{d}\theta(\mathbf{x}-\mathbf{x}')}{\mathrm{d}t} B'_\mathrm{n}\, \mathrm{d}^2x', \tag{1}$$

where B_n is the normal component of the magnetic field $\mathbf{B}$, S_p is the surface over which the helicity is estimated (here, the photosphere), and the rotation rate $\mathrm{d}\theta(\mathbf{x}-\mathbf{x}')/\mathrm{d}t$ of a couple of points $\mathbf{x}$ and $\mathbf{x}'$, is given by:

$$\frac{\mathrm{d}\theta(\mathbf{x}-\mathbf{x}')}{\mathrm{d}t} = \frac{[(\mathbf{x}-\mathbf{x}')\times(\mathbf{u}-\mathbf{u}')]_n}{|\mathbf{x}-\mathbf{x}'|^2}. \tag{2}$$

The velocity field $\mathbf{u}$, called "flux transport velocity," (Welsch, 2006) corresponds to the motions of the magnetic structure at the photospheric surface.

A key aspect of the derivation of the helicity injection is to properly derive the flux-transport velocity field $\mathbf{u}$. A larger and larger number of velocity-inversion techniques now exist to derive the motion of magnetic features at the solar surface (Welsch *et al.*, 2007; Chae and Sakurai, 2008). Methods based on local correlation tracking (LCT) (November and Simon, 1988) were used extensively to derive the helicity injection in ARs (*e.g.*, Chae, 2001; Nindos, Zhang, and Zhang, 2003; Pariat *et al.*, 2006; Jeong and Chae, 2007). However, Schuck (2005) clearly demonstrated that the local correlation tracking was inconsistent with the magnetic induction equation. Schuck (2006) proposed an improved method, the differential affine velocity estimator (DAVE), which uses a variational principle to minimize deviations in the magnitude of the magnetic induction equation constrained by an affine velocity profile. DAVE was particularly efficient at determining the correct helicity values in a test case using numerically simulated data, compared to the more traditional LCT method (Welsch *et al.*, 2007).

Even though DAVE4VM, an improved method using vector magnetograms as input, was developed by Schuck (2008), in the present article we use the DAVE algorithm since only line-of-sight magnetograms are available. In order to determine the velocity flux, we use the 96-min cadence MDI full-disk magnetograms. We select a portion of MDI magnetograms with a field-of-view of $477'' \times 457'' = 346$ Mm $\times$ 332 Mm centered on the AR. These sections are large enough to assume that the AR is isolated from other ARs in the helicity computation. We remove solar differential rotation by taking, as a reference time, the moment when the AR crosses the central meridian. Following LaBonte, Georgoulis, and Rust (2007), we correct the magnetic field by a factor of 1.56 (as recommended by Berger and Lites, 2003) and we multiply the line-of-sight field by the secant of the angle corresponding to the location of the center of the AR relative to the disk center, so as to obtain an approximation of the normal component of the field at each time. In order to limit the errors due to strong geometrical deformation induced by the projection of the AR on the observation

plane, we determine the helicity flux only when the AR is within a radius of 41° from the solar disk center. Therefore, we can compute the helicity accumulation only after 16 November, 11:11 UT, *i.e.*, two days before the flares. To derive the velocity field with DAVE we use a window size of $\omega_0 = 11$ pixels, as suggested by Schuck (2006) for optimum performance.

5.2. Helicity Flux

The traditional diagnostic to estimate the magnetic helicity in an AR is to compute the accumulated helicity. The helicity flux $\mathrm{d}H/\mathrm{d}t$ can then be simply estimated by integrating G_θ over S_p, whereas the helicity accumulation, ΔH, between two times t_i and t_f can be determined by the time integration of the helicity flux:

$$\left.\frac{\mathrm{d}H}{\mathrm{d}t}\right|_{\mathcal{S}_\mathrm{p}} = \int_{S_\mathrm{p}} G_\theta \, \mathrm{d}^2x \quad \text{and} \quad \Delta H = \int_{t_\mathrm{i}}^{t_\mathrm{f}} \left.\frac{\mathrm{d}H}{\mathrm{d}t}\right|_{\mathcal{S}_\mathrm{p}} dt, \tag{3}$$

with t_i and t_f the initial and final times, respectively.

In order to control the errors in the estimation of **u**, we use different values of $\omega = 13$, 15, and 19 pixels. We find that the mean variation for the whole helicity computation (while the AR has an heliocentric angle of 41°) is about 0.8×10^{21} Wb^2 s^{-1}. We also perform helicity computations after introducing a random uniform noise of 20 G or 50 G in the magnetograms. The former is of the order of the noise levels in MDI measurements, while the latter is larger than those (Scherrer *et al.*, 1995). We find that they induce a mean variation of 0.3×10^{21} and 0.8×10^{21} Wb^2 s^{-1}, respectively, relative to the original data. However, this does not warrant incorrect estimations inherent in the poor temporal resolution (96 min!) and to the intrinsic use of the flux-transport velocity **u** (*e.g.*, Démoulin and Berger, 2003; Welsch *et al.*, 2007; Démoulin and Pariat, 2009). Given these uncertainties, the measured helicity flux and helicity are shown in Figure 8.

The main result of the helicity flux estimation confirms the results of the topological (Section 4) and morphological (Section 3) analysis of AR 10501: negative injection of helicity is dominant. In the two days preceding the flares, more than -4×10^{26} Wb^2 (-4×10^{42} Mx^2) are injected in the AR. The helicity accumulation profile presents two stages, first a relatively

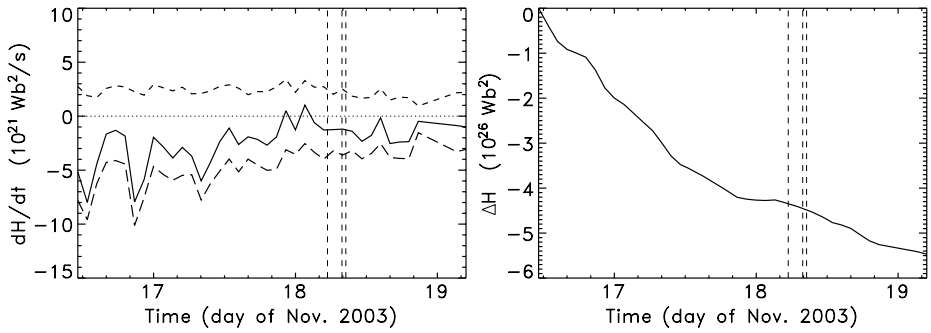

Figure 8 Signed and total helicity fluxes (left) and accumulated helicity (right) in AR 10501 between 16 November 11:11 UT and 19 November 04:51 UT. The vertical dashed lines correspond to the time of the peak intensity of the three flares described in Section 2. In the left panel, the positive helicity flux (short-dashed line) corresponds to the integrated helicity density of positive sign while the negative helicity flux (long-dashed line) corresponds to the integrated helicity density of negative sign. The total helicity flux (continuous line) is the sum of the signed fluxes.

constant injection at a rate of the order of -8×10^{24} Wb^2 hr^{-1} and second, a relatively constant flux a few hours before the eruption. This agrees with previous studies of intense flaring regions (Park *et al.*, 2008). AR 10501 is a mature region; therefore, a much larger amount of helicity was probably injected before. Most intensely flaring ARs have a helicity larger than 10^{26} Wb^2 (LaBonte, Georgoulis, and Rust, 2007) with an average helicity for erupting regions of about 13×10^{26} Wb^2 (measured from the emergence of AR by Nindos and Andrews, 2004; however, we corrected an erroneous factor of 2 in their Equation (1)). There is, therefore, enough helicity to generate a CME and an MC for which the average helicity is estimated to be about 10^{26} Wb^2 (*e.g.*, DeVore, 2000; Lynch *et al.*, 2005). However, the problem remains that the helicity accumulation of the AR is opposite to the MC, in strong contradiction with what is expected (cf. Section 1)!

How significant is the positive helicity injection? In Figure 8 we observe that, although the negative helicity injection (long-dashed curve) is largely dominant on 16 November, it seems to decrease by the end of 17 November. The positive injection is even slightly dominant a few hours before the flares. However, the total helicity flux values lie within the error margin and are below the noise threshold. Different choices of ω with DAVE sometimes present no dominance of positive helicity. Therefore, it is a strong overstatement to sustain that there is dominance of positive helicity a few hours before the flare. We also do not see any particular change of the sign of the helicity flux during these flares.

Nonetheless, a particular characteristic of the helicity injection in AR 10501 is that both positive and negative fluxes of helicity tend to be large compared to the total helicity flux. The injection of positive helicity (short-dashed curve, Figure 8, left panel) is relatively constant and is in the range $2-3 \times 10^{21}$ Wb^2 s^{-1}. Is this flux injection due to a localized injection of helicity? If confirmed, this can result in a helicity accumulation larger than 4×10^{26} Wb^2, which can be sufficient to explain the generation of a positive helicity MC.

However, one must be extremely careful when studying positive and negative helicity fluxes separately since the methods used to estimate the helicity may produce artifacts. Pariat, Démoulin, and Berger (2005) demonstrated that the previous definition for the helicity density, called G_A, requiring the computation of the vector potential of the potential magnetic field $\mathbf{A}_\mathrm{p}$, leads to the generation of strong spurious signals of the opposite helicity sign. Pariat, Démoulin, and Berger (2005) defined a new helicity density, G_θ, used in the present study, that significantly reduced the intensity of the fake helicity fluxes. Applying this new definition to ARs, Pariat *et al.* (2006) showed that the intensity of the non-dominant fluxes were reduced and that the helicity injection was much more uniform and unipolar (*i.e.*, of only one sign) than previously found. However, G_θ, as a proxy for the helicity flux density, is not exempt of spurious signals (Pariat, Démoulin, and Nindos, 2007). It is, therefore, necessary to do a careful analysis of the helicity density map to determine if the local helicity fluxes are real or not.

6. Local Injection of Magnetic Helicity in AR 10501

6.1. Helicity Flux Maps

The helicity flux distribution estimated with G_θ is displayed in Figure 9 at several times before the flares. As expected, the maps are strongly dominated by negative helicity patches, the main one being located in the central intense negative polarity N1 (see Figure 5). The magnitude of helicity density is typically of 15×10^6 Wb^2 m^{-2} s^{-1} at that location. This is two times larger than the typical flux density in the surrounding polarities (N2/P2; N3/P3)

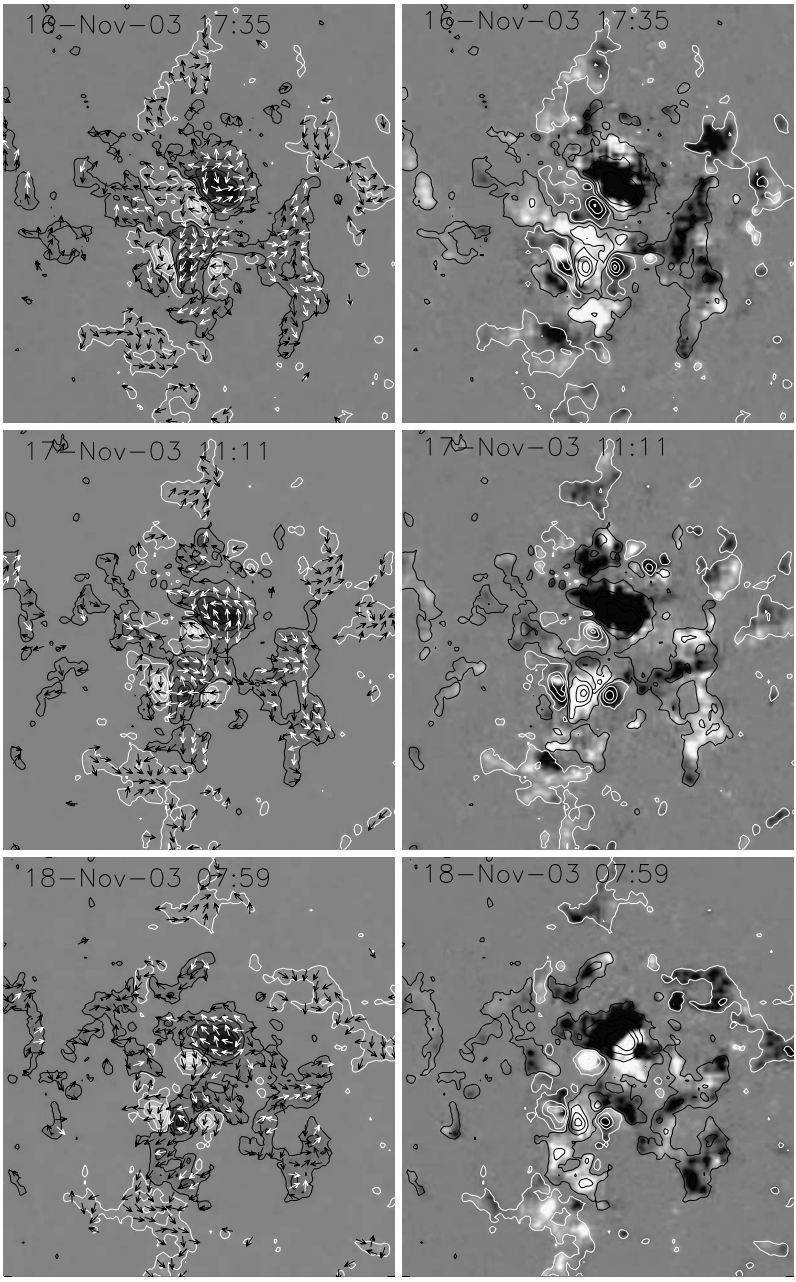

Figure 9 Evolution of the magnetic field and of the helicity injection in AR 10501 on November 2003. The field-of-view is of $279'' \times 299'' = 202$ Mm $\times$ 217 Mm. Left panels: line-of-sight (B_n) MDI magnetograms with flux transport velocity field **u** (arrows). Right panels: helicity flux density (G_θ) maps. Note that the saturation level, equal to 10^6 Wb^2 m^{-2} s^{-1}, has been chosen to enhance the distribution of helicity in the magnetic polarities of intermediate intensity. The contours correspond to 100, 600, 1200, 1800 G (white for positive and black for negative polarities).

and about one order of magnitude larger than in the southern polarities (N4/P4), where the absolute flux densities are of the order of 2×10^6 Wb^2 m^{-2} s^{-1}.

Even though the maps are dominated by the negative injection in N1, we observe positive patches in the south of the AR, around the polarities P2/N2, P3/N3, and P4/N4 (see Figure 9). These positive patches have a lower intensity, but are more extended than the one in N1 corresponding to the main helicity injection. In addition, even if extended patches of positive helicity flux are observed, patches of negative helicity flux are present nearby. So what is the real helicity flux injection in this area? Are all these patches real or spurious signals?

Methods estimating the helicity flux fail to produce fully reliable helicity flux density maps because the helicity flux density per unit surface (as G_A and G_θ) is not a physically meaningful quantity. Magnetic helicity flux density can only be properly defined for an elementary flux tube (Pariat, Démoulin, and Berger, 2005). The physically meaningful helicity flux density through a surface is the helicity flux density per unit flux, *i.e.*, the weighted sum of helicity injected at both footpoints of a magnetic field line. The proxy G_θ only represents a particular distribution of the helicity injected in an elementary flux tube over its footpoint. To properly determine the helicity flux injection it is, therefore, necessary to have a knowledge of the field line connectivity. Summing the helicity injection in a connectivity domain is one way to obtain correct information about the helicity flux. Therefore, in order to estimate the helicity flux in the southern polarities we need to determine their connectivity before the flare.

6.2. Localized Helicity Injection

TRACE images (for example see Figure 3, bottom panel) give little information about the real connectivity around polarities P2/N2, P3/N3, and P4/N4. Therefore, we use the extrapolation (Section 4) to estimate the connectivity of the negative polarities. We use the magnetic field model with $\alpha = -1.2 \times 10^{-2}$ Mm^{-1} computed from the MDI magnetogram at 06:23 UT just prior to the flare. We assume that it accurately represents the connectivity during the previous two days, *i.e.*, we suppose that extremely limited reconnection has occurred that will change the connectivity. We also perform an extrapolation with $\alpha = 1.2 \times 10^{-2}$ Mm^{-1}. We observe that the field line connectivity is relatively insensitive to the variation of α. This is not surprising since field lines anchored in the negative polarities are relatively short and the variation of α primarily affects field lines with lengths of the order of α^{-1}, as previously discussed. Nonetheless, this connectivity conservation in spite of the change in α gives us confidence in our following results.

We determine the existence of three connectivity domains around P2/N2, P3/N3, and P4/N4 (see Figure 10). Whereas P4 and N4 are simply connected, we observe that field lines originating from N2 and N3 actually split between P2 and P3. A (quasi-) separatrix is likely to lie in the middle of N2 and N3. The three connectivity domains are thus the one associated with P2 (blue lines on Figure 10), the one associated with P3 (pink lines on Figure 10), and the P4/N4 one (green lines on Figure 10).

Given the connectivity, we are able to estimate the helicity in each domain. We roughly approximate these domains as rectangular submaps of the MDI magnetograms, *i.e.*, these submaps are delimited by eye in order to fit the domain in the extrapolation. We do not believe that a more sophisticated method is necessary given the uncertainty in the extrapolation and the fact that we mostly want an estimate of the total helicity flux in each of these domains. We, nonetheless, control the amount of magnetic flux unbalance in each

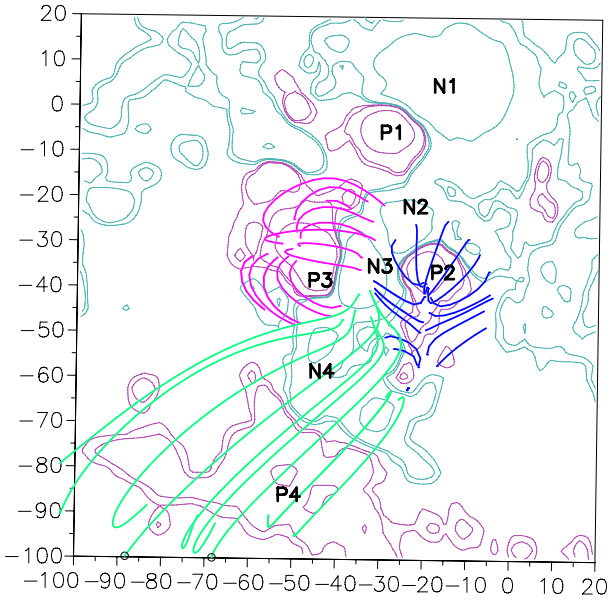

Figure 10 Field lines (06:23 UT) computed to show the three connectivity domains around polarities N2/P2, N3/P3 and N4/P4. Each set of field lines (different colors) presents a different connectivity domain: The P2 domain is displayed with blue lines, the P3 domain with pink lines and the P4/N4 domain with green lines.

of these domains. Balanced magnetic flux indeed implies that the boundaries of our domains are well defined (in a given domain the flux should be perfectly balanced by definition). In none of the computed domains do we find a contrast, C, larger than 0.2, with $C = (|\Phi_+| - |\Phi_-|)/(|\Phi_+| + |\Phi_-|)$, with $|\Phi_\pm|$ the total positive (negative) flux.

Integrating the helicity flux density in each of these connectivity domains, we confirm the result that a positive helicity injection occurred in the southern polarities. More precisely, we find that, in the P3 domain, the helicity injection is extremely mixed. Strong patches of both signs are present. The helicity accumulation is first negative (-4×10^{24} Wb^2), then it becomes positive (9×10^{24} Wb^2) between 00:00 UT and 17:35 UT on 17 November, only to return to be slightly negative after. In the P2 connectivity domain the helicity injection is more clearly positive. However, the accumulated helicity is not larger than 5×10^{24} Wb^2 during the two days preceding the flaring events.

Actually, the largest positive helicity injection is found to occur in the third domain, P4/N4. Even though the helicity flux density is relatively small, this is the region where a much extended patch of positive helicity flux is observed. Even though the computed helicity density is low, we can confirm that the helicity computations with different values of ω and noise do not sensitively change the results. We determine that in P4/N4 a total helicity larger than 30×10^{24} Wb^2 was injected between 16 November 11:11 UT and 18 November 07:59 UT (see Figure 11). Should this injection occur over six days at the same rate an accumulated helicity of the order of 10^{26} Wb^2 will be injected, enough to explain the helicity carried by the positive MC.

Studying the flux transport velocity field **u**, it is also possible to understand why positive injection occurs there. Two kinds of motion in the photospheric magnetic polarities occur at the location of N4/P4. First, there is a global southward displacement of P4 and N4 (see Figure 9, left panels). However, we see that this displacement is more pronounced for P4. Second, following isocontours of the magnetic field, we observe that N4 and P4 have a relative converging motion. This motion cannot plausibly inject a large amount of helicity. However, we also observe in Figure 9, that **u** presents a dominant west orientation in P4.

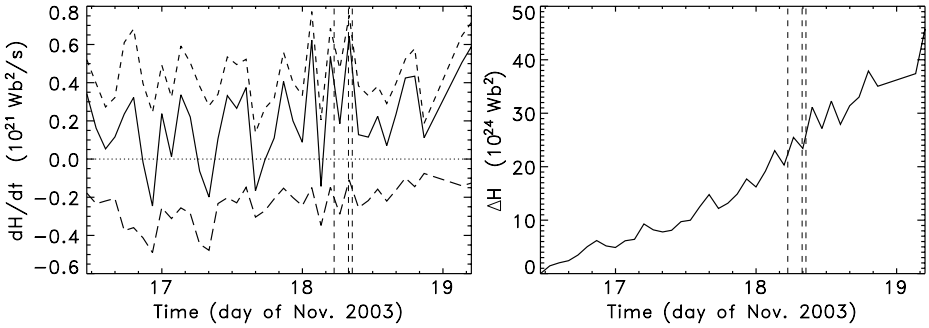

Figure 11 Positive (dashed), negative (long-dashed), and total (solid) helicity fluxes (left) and accumulated helicity (right) in N4/P4 domain of AR 10501 between 16 November 11:11 UT and 19 November 04:51 UT. The description of the figure is the same as in Figure 8

This reveals the fact that P4 is actually rotating westward relative to N4. A counterclockwise rotation of a positive polarity around a negative polarity (injecting positive helicity) is perfectly consistent with the helicity injection measured in N4/P4.

Overall, the careful study of the helicity density maps allows us to confirm that, even if AR 10501 presents a global negative helicity, a localized positive injection occurs at the south of the main AR spot, at the location of polarities N4/P4, precisely where an erupting segment of the filament is rooted.

7. Conclusion

We determine the global and local magnetic helicity sign of AR 10501 on 18 November 2003 using different methods based on the analysis of a multiwavelength data set. We also discuss the association of this AR with the MC of 20 November 2003, observed by ACE, the largest geoeffective cloud during Solar Cycle 23.

AR 10501 is surrounded by a large apparently circular-shaped single filament, which is in fact formed by several distinct segments. The flares of 18 November 2003 are initiated by the continuous emergence of magnetic bipoles and by the eruption of some segments of the filament. The destabilization of one of the filament segments is the primary trigger of the third flare. As discussed in the "CSHKP" (Carmichael, 1964; Sturrock, 1966; Hirayama, 1974, and Kopp and Pneuman, 1976; also Forbes and Malherbe, 1991) standard solar-flare model, a filament eruption (in our particular case, the eruption of a filament segment) due to some magnetic instability occurs above the magnetic inversion line. As a result, filament material moves away from the solar surface, the pre-existing magnetic arcade stretches upward, and the condition arises for magnetic reconnection, thus leading to a CME and a subsequent MC in the interplanetary medium.

Based on the multiwavelength data set, we find the following results in relation to the magnetic helicity of the AR:

– The very extended filament within and surrounding the AR presents evidence of dextral, as well as sinistral, chirality, *i.e.*, negative and positive magnetic helicity.
– The sunspot whorls show a left-hand twist, which corresponds to negative magnetic helicity.
– The reverse-J-shaped flare ribbons indicate negative helicity in the active region. However, this may be a false indicator because the ribbons follow the magnetic inversion line.

– From the coronal magnetic field model, we find that the best α values to fit the large-scale TRACE loops are negative. These negative α values mean that the magnetic helicity is globally negative. However, at the south of the AR, where N4/P4 lie, the value of α needed to locally match the shape of loops in the post-flare arcade after the flare that peaked at 08:31 UT has a tendency to be positive toward east and negative toward west, in agreement with the location of sinistral and dextral filament segments.
– The computation of the magnetic helicity injection, using G_θ maps, indicates that the main spot in the AR is dominated by negative helicity. However, there is a strong local positive injection of helicity in the southern polarities (N4/P4) of the AR.

From the above evidences we conclude that AR 10501 has a global negative magnetic helicity. Despite this global negative helicity, the helicity density maps, *i.e.*, G_θ maps, show a strong injection of positive magnetic helicity in the southern polarities. Our results provide a clear example of an AR in which the magnetic helicity sign is mixed, with a simultaneous injection of both helicity signs. Previous work (Pevtsov, Canfield, and McClymont, 1997; Green *et al.*, 2002) already reported examples in which the total helicity sign of an AR changed as it evolved because of parasitic magnetic polarity emergence having an opposite helicity sign to the main one. This is the first time that helicity flux density maps bring new information about the local helicity injection into an active region whose sign is opposite to the global helicity of the AR. A similar local injection of helicity of an opposite sign may explain the few cases of discrepancy found by Leamon *et al.* (2004) between the helicity sign carried by MCs and the global helicity sign of their identified solar source region.

We speculate that, due to a global instability in the AR, a flux rope with positive helicity erupted. This flux rope will contain the filament segment with positive helicity. As discussed previously, the erupting filament has sections with opposite chiralities (sinistral in F2a and dextral in F2b). Filaments with the same chirality can merge, while those with different chirality cannot merge (Martin, 1998; Rust, 2001; Schmieder *et al.*, 2004; Aulanier, DeVore, and Antiochos, 2006). The segment F2 corresponds to two different flux tubes having the same axial magnetic field direction, in agreement with the counterstreaming motions observed before the eruption. However, the two sections F2a and F2b have opposite chiralities. Possibly, during the third flare, these two segments interacted through magnetic reconnection and helicity carried by both sections partially canceled. The positive helicity carried by F2a being larger, the CME and ICME induced by the eruption transported away a net-positive helicity, as measured by ACE at 1 AU (Gopalswamy *et al.*, 2005).

Finally, our finding of a local injection of helicity with opposite signs is potentially important for eruption models. Kusano *et al.* (2004) developed a model based on the reconnection of magnetic flux ropes with opposite helicity. Helicity annihilation potentially allows the release of a larger amount of free energy since the field can eventually relax to a state closer to potential.

Acknowledgements The authors thanks Dr. Pascal Démoulin for fruitful discussions and suggestions. R.C. thanks *Le Centre Franco-Indien pour la Promotion de la Recherche Avancée* (CEFIPRA) for his post-doctoral grant. This work was done in the frame of the European network SOLAIRE. This work uses the DAVE/DAVE4VM codes written and developed by the Naval Research Laboratory. E.P. wishes to thank Peter Schuck for providing the DAVE/DAVE4VM code and for useful discussions. The work of E.P. was supported, in part, by the NASA HTP and SR&T programs. C.H.M. thanks the Argentinean grants: UBA-CyT X127 and PICT 03-33370 (ANPCyT). C.H.M. is a member of the *Carrera del Investigador Científico*, CONICET. We acknowledge the use of TRACE data. MDI data are a courtesy of SOHO/MDI consortium. SOHO is a project of international cooperation between ESA and NASA. B.S and C.H.M started this work in the frame of the ISSI workshop chaired by Dr. Consuelo Cid (2008 – 2010). We also thank the anonymous referee for helpful and constructive comments.

References

Ali, S.S., Uddin, W., Chandra, R., Mary, D.L., Vršnak, B.: 2007, *Solar Phys.* **240**, 89.
Aulanier, G., DeVore, C.R., Antiochos, S.K.: 2006, *Astrophys. J.* **646**, 1349.
Berger, M.A.: 1984, *Geophys. Astrophys. Fluid Dyn.* **30**, 79.
Berger, T.E., Lites, B.W.: 2003, *Solar Phys.* **213**, 213.
Berger, M.A., Ruzmaikin, A.: 2000, *J. Geophys. Res.* **105**, 10481.
Bobra, M.G., van Ballegooijen, A.A., DeLuca, E.E.: 2008, *Astrophys. J.* **672**, 1209.
Bothmer, V., Schwenn, R.: 1994, *Space Sci. Rev.* **70**, 215.
Bothmer, V., Schwenn, R.: 1998, *Ann. Geophys.* **16**, 1.
Brueckner, G.E., Howard, R.A., Koomen, M.J., Korendyke, C.M., Michels, D.J., Moses, J.D., *et al.*: 1995, *Solar Phys.* **162**, 357.
Burlaga, L., Sittler, E., Mariani, F., Schwenn, R.: 1981, *J. Geophys. Res.* **86**, 6673.
Carmichael H.: 1964, In: Hess, W.N. (ed.) *The Physics of Solar Flares, NASA*, *SP-50*, 451.
Chae, J.: 2001, *Astrophys. J.* **560**, L95.
Chae, J., Sakurai, T.: 2008, *Astrophys. J.* **689**, 593.
Chae, J., Wang, H., Qiu, J., Goode, P.R., Strous, L., Yun, H.S.: 2001, *Astrophys. J.* **560**, 476.
Chandra, R., Schmieder, B., Aulanier, G., Malherbe, J.M.: 2009, *Solar Phys.* **258**, 53.
Dasso, S., Gulisano, A.M., Mandrini, C.H., Démoulin, P.: 2005, *Adv. Space Res.* **35**, 2172.
Dasso, S., Mandrini, C.H., Démoulin, P., Luoni, M.L.: 2006, *Astron. Astrophys.* **455**, 349.
Démoulin, P.: 2007, *Adv. Space Res.* **39**, 1674.
Démoulin, P.: 2008, *Ann. Geophys.* **26**, 3113.
Démoulin, P., Berger, M.A.: 2003, *Solar Phys.* **215**, 203.
Démoulin, P., Pariat, E.: 2009, *Adv. Space Res.* **43**, 1013.
Démoulin, P., Priest, E.R., Lonie, D.P.: 1996, *J. Geophys. Res.* **101**, 7631.
Démoulin, P., Bagala, L.G., Mandrini, C.H., Henoux, J.C., Rovira, M.G.: 1997, *Astron. Astrophys.* **325**, 305.
Démoulin, P., Mandrini, C.H., van Driel-Gesztelyi, L., Thompson, B.J., Plunkett, S., Kovári, Z., Aulanier, G., Young, A.: 2002, *Astron. Astrophys.* **382**, 650.
Deng, Y., Lin, Y., Schmieder, B., Engvold, O.: 2002, *Solar Phys.* **209**, 153.
DeVore, C.R.: 2000, *Astrophys. J.* **539**, 944.
DeVore, C.R., Antiochos, S.K., Aulanier, G.: 2005, *Astrophys. J.* **629**, 1122.
Dudík, J., Aulanier, G., Schmieder, B., Bommier, V., Roudier, T.: 2008, *Solar Phys.* **248**, 29.
Forbes, T.G., Malherbe, J.M.: 1991, *Solar Phys.* **135**, 361.
Gopalswamy, N., Yashiro, S., Michalek, G., Xie, H., Lepping, R.P., Howard, R.A.: 2005, *Geophys. Res. Lett.* **32**, 12.
Green, L.M., López Fuentes, M.C., Mandrini, C.H., Démoulin, P., Van Driel-Gesztelyi, L., Culhane, J.L.: 2002, *Solar Phys.* **208**, 43.
Handy, B.N., Acton, L.W., Kankelborg, C.C., Wolfson, C.J., Akin, D.J., Bruner, M.E., *et al.*: 1999, *Solar Phys.* **187**, 229.
Hirayama, T.: 1974, *Solar Phys.* **34**, 323.
Jeong, H., Chae, J.: 2007, *Astrophys. J.* **671**, 1022.
Klein, L.W., Burlaga, L.F.: 1982, *J. Geophys. Res.* **87**, 613.
Kopp, R.A., Pneuman, G.W.: 1976, *Solar Phys.* **50**, 85.
Kusano, K., Maeshiro, T., Yokoyama, T., Sakurai, T.: 2004, *Astrophys. J.* **610**, 537.
LaBonte, B.J., Georgoulis, M.K., Rust, D.M.: 2007, *Astrophys. J.* **671**, 955.
Leamon, R.J., Canfield, R.C., Jones, S.L., Lambkin, K., Lundberg, B.J., Pevtsov, A.A.: 2004, *J. Geophys. Res.* **109**, 5106.
Lim, E.K., Chae, J.: 2009, *Astrophys. J.* **692**, 104.
Lim, E.K., Jeong, H., Chae, J., Moon, Y.J.: 2007, *Astrophys. J.* **656**, 1167.
Low, B.C.: 1996, *Solar Phys.* **167**, 217.
Luoni, M.L., Mandrini, C.H., Dasso, S., van Driel-Gesztelyi, L., Démoulin, P.: 2005, *J. Atmos. Solar-Terr. Phys.* **67**, 1734.
Lynch, B.J., Gruesbeck, J.R., Zurbuchen, T.H., Antiochos, S.K.: 2005, *J. Geophys. Res.* **110**, 8107.
Mandrini, C.H., Pohjolainen, S., Dasso, S., Green, L.M., Démoulin, P., van Driel-Gesztelyi, L., Copperwheat, C., Foley, C.: 2005, *Astron. Astrophys.* **434**, 725.
Martin, S.F.: 1998, *Solar Phys.* **182**, 107.
Martin S.F., Bilimoria R., Tracadas P.W.: 1994, In: Rutten, R.J., Schrijver, C.J. (eds.) *Solar Surface Magnetism*, Kluwer Academic, Dordrecht, 303.
Marubashi, K.: 1997, In: Crooker, N., Joselyn, J.A., Feynmann, J. (eds.) *Coronal Mass Ejections*, *Geophys. Monogr. Ser.* **99**, AGU, Washington, 147.

Moštl, C., Miklenic, C., Farrugia, C.J., Temmer, M., Veronig, A., Galvin, A.B., Vrsnak, B., Biernat, H.K.: 2008, *Ann. Geophys.* **26**, 3139.
Nakagawa, Y., Raadu, M.A., Billings, D.E., McNamara, D.: 1971, *Solar Phys.* **19**, 72.
Nakwacki, M., Dasso, S., Mandrini, C., Demoulin, P.: 2008, *J. Atmos. Solar-Terr. Phys.* **70**, 1318.
Nindos, A., Andrews, M.D.: 2004, *Astrophys. J.* **616**, L175.
Nindos, A., Zhang, H.: 2002, *Astrophys. J.* **573**, L133.
Nindos, A., Zhang, J., Zhang, H.: 2003, *Astrophys. J.* **594**, 1033.
November, L.J., Simon, G.W.: 1988, *Astrophys. J.* **333**, 427.
Pariat, E., Démoulin, P., Berger, M.A.: 2005, *Astron. Astrophys.* **439**, 1191.
Pariat, E., Démoulin, P., Nindos, A.: 2007, *Adv. Space Res.* **39**, 1706.
Pariat, E., Nindos, A., Démoulin, P., Berger, M.A.: 2006, *Astron. Astrophys.* **452**, 623.
Park, S.H., Lee, J., Choe, G.S., Chae, J., Jeong, H., Yang, G., Jing, J., Wang, H.: 2008, *Astrophys. J.* **686**, 1397.
Pevtsov, A.A., Canfield, R.C., Zirin, H.: 1996, *Astrophys. J.* **473**, 533.
Pevtsov, A.A., Canfield, R.C., McClymont, A.N.: 1997, *Astrophys. J.* **481**, 973.
Régnier, S., Amari, T., Canfield, R.C.: 2005, *Astron. Astrophys.* **442**, 345.
Rompolt, B.: 1990, *Hvar Obs. Bull.* **14**, 37.
Rust, D.M.: 1994, *Geophys. Res. Lett.* **21**, 241.
Rust, D.M.: 2001, *J. Geophys. Res.* **106**, 25075.
Rust, D.M., Kumar, A.: 1994, *Solar Phys.* **155**, 69.
Rust D.M., Martin S.F.: 1994, In: Balasubramaniam, K.S., Simon, G.W. (eds.) *Solar Active Region Evolution: Comparing Models with Observations* **CS-68**, Astron. Soc. Pac., San Francisco, 337.
Rust, D.M., Anderson, B.J., Andrews, M.D., Acuña, M.H., Russell, C.T., Schuck, P.W., Mulligan, T.: 2005, *Astrophys. J.* **621**, 524.
Ruzmaikin, A., Martin, S., Hu, Q.: 2003, *J. Geophys. Res.* **108**, 1096.
Scherrer, P.H., Bogart, R.S., Bush, R.I., Hoeksema, J.T., Kosovichev, A.G., Schou, J., *et al.*: 1995, *Solar Phys.* **162**, 129.
Schmieder, B., van Driel-Gesztelyi, L.: 2005, In: Dere, K., Wang, J., Yan, Y. (eds.) *Coronal and Stellar Mass Ejections, IAU Symp.* **226**, 149.
Schmieder, B., Mein, N., Deng, Y., Dumitrache, C., Malherbe, J.M., Staiger, J., Deluca, E.E.: 2004, *Solar Phys.* **223**, 119.
Schmieder, B., Gunár, S., Heinzel, P., Anzer, U.: 2007, *Solar Phys.* **241**, 53.
Schmieder, B., Bommier, V., Kitai, R., Matsumoto, T., Ishii, T.T., Hagino, M., Li, H., Golub, L.: 2008, *Solar Phys.* **247**, 321.
Schuck, P.W.: 2005, *Astrophys. J.* **632**, L53.
Schuck, P.W.: 2006, *Astrophys. J.* **646**, 1358.
Schuck, P.W.: 2008, *Astrophys. J.* **683**, 1134.
Sturrock, P.A.: 1966, *Nature* **211**, 695.
Subramanian, P., Dere, K.P.: 2001, *Astrophys. J.* **561**, 372.
Tandberg-Hanssen E.: 1994, *The Nature of Solar Prominences*, Kluwer Academic, Dordrecht, 113.
Wang, Y., Zhou, G., Ye, P., Wang, S., Wang, J.: 2006, *Astrophys. J.* **651**, 1245.
Watari, S., Watanabe, T., Marubashi, K.: 2001, *Solar Phys.* **202**, 363.
Welsch, B.T.: 2006, *Astrophys. J.* **638**, 1101.
Welsch, B.T., Abbett, W.P., DeRosa, M.L., Fisher, G.H., Georgoulis, M.K., Kusano, K., Longcope, D.W., Ravindra, B., Schuck, P.W.: 2007, *Astrophys. J.* **670**, 1434.
Yurchyshyn, V., Hu, Q., Abramenko, V.: 2005, *Space Weather* **3**, 8.
Yurchyshyn, V.B., Wang, H., Goode, P.R., Deng, Y.: 2001, *Astrophys. J.* **563**, 381.
Yurchyshyn, V., Liu, C., Abramenko, V., Krall, J.: 2006, *Solar Phys.* **239**, 317.
Zirker, J.B., Martin, S.F., Harvey, K., Gaizauskas, V.: 1997, *Solar Phys.* **175**, 27.